International Journal of Mechanical Engineering and Applications
2023; 11(4): 81-93
http://www.sciencepublishinggroup.com/j/ijmea
doi: 10.11648/j.ijmea.20231104.12
ISSN: 2330-023X (Print); ISSN: 2330-0248 (Online)

Processing and Characterization of Maraging Steel Using LPBF Additive Manufacturing Technology

Ramesh Kumar Saride[1, *], Srinivas Vajjala[1], Aman Kumar[2], Rajesh Kumar[1], Laxminarayana Pappula[3], Jagan Reddy Ginuga[1]

[1]Defence Metallurgical Research Laboratory, Hyderabad, India

[2]Jindal Stainless Limited, Jajpur, India

[3]Department of Mechanical Engineering, Osmania University College of Engineering, Osmania University, Hyderabad, India

Email address:

srameshkumar.dmrl@gov.in (Ramesh Kumar Saride), srinivasv.dmrl@gov.in (Srinivas Vajjala), aman209458@gmail.com (Aman Kumar), rajesh.dmrl@gmail.com (Rajesh Kumar), laxp@osmania.ac.in (Laxminarayana Pappula), ginugajagan_61@yahoo.co.in (Jagan Reddy Ginuga)

[*]Corresponding author

To cite this article:

Ramesh Kumar Saride, Srinivas Vajjala, Aman Kumar, Rajesh Kumar, Laxminarayana Pappula, Jagan Reddy Ginuga. Processing and Characterization of Maraging Steel Using LPBF Additive Manufacturing Technology. *International Journal of Mechanical Engineering and Applications*. Vol. 11, No. 4, 2023, pp. 81-93. doi: 10.11648/j.ijmea.20231104.12

Received: July 22, 2023; **Accepted**: August 8, 2023; **Published**: August 22, 2023

Abstract: Manufacturing processes saw significant change with the advent of Additive manufacturing (AM), which enables manufacture of complex shaped components, light-weight designs with reduced manufacturing lead times. Production of components in Maraging steel using Laser Powder Bed fusion Technology (LPBF) AM technique has gained importance in recent times, especially in defence & aerospace sectors. Current work entails processing and characterization of Maraging Steel fabricated through LPBF technology. Using full factorial DoE, primary process parameters were identified as Laser Power - 200W, Scan speed - 800mm/sec, Hatch width - 80µm. A process window comprising of laser power and scan speed was identified corresponding to the region with an energy density of ~100J/mm^3. Microstructural characterization of as-deposited (AD), solution treated (ST) and ST+Aged (STA) specimens using optical and SEM microscopy revealed presence of defects like lack-of-fusion, soot and spatter. Additionally, specimens were printed with modified process parameters with zig-zig scanning pattern, resulted in reduction of defects. Furthermore, micro-hardness and tensile properties have been evaluated in AD, ST and STA conditions. The tensile strength of AD is higher compared to wrought material, whereas, STA showed equivalent strength. Also, it was inferred that printing in horizontal orientation is preferable to attain higher tensile properties.

Keywords: Additive Manufacturing, Laser Powder Bed Fusion, Maraging Steel, Microstructural Characterization, Porosity

1. Introduction

Maraging steels may be classified as ultra-high-strength carbon-free steels, which offer an unusual combination of very high tensile strength with good fracture toughness. The term “maraging” refers to the martensite age-hardening process that takes place in a martensite matrix in the absence of carbon. The rare combination of high strength and toughness found with maraging steel makes it well suited for safety-critical aerospace & aircraft structures such as rocket motor cases, landing gears, helicopter undercarriages that require high strength and also damage tolerance. The massive increase in strength is associated with precipitation hardening caused by nanometric sized intermetallic particles that precipitate during subsequent aging of martensite in the temperature range of 400-600°C. During the solidification of liquid metal to solid ingot at RT condition, soft BCC martensitic structure of iron-nickel with supersaturated cobalt and molybdenum solid solution is obtained. Subsequent aging treatment at a suitable

temperature and time hardens the matrix due to the formation of Ni-Mo, Ni-Ti and Fe-Mo, based nano-sized intermetallic precipitates in the martensitic structure.

Additive manufacturing (AM), which is also commonly known as 3D Printing is gaining much importance in the production of complex engineering components with high dimensional accuracy, especially in the defence, aerospace and aircraft industry. AM is a process of building 3D solid parts layer-by-layer virtually of any shape from a digital model. Additive manufacturing has many advantages over the traditional manufacturing methodologies like improving functional performance/efficiency, realise complex designs, weight reduction, multiple prototypes/designs, reduced lead time etc., [1]. AM comes as a ready solution to manufacture the components as conceptualized, designed and modeled by the designer. This technology enables the manufacturers to create components with geometry which was very difficult or expensive or cannot be manufactured by other means. It allows the engineers to replace complex assemblies with unified parts that are lighter than previous designs and saving weight [2].

Good weldability with superior strength, fracture toughness and low specific weight of Maraging steel 300 (M300) makes it a suitable candidate for producing complex aerospace components using additive manufacturing technology. Additive manufacturing of M300 is therefore an important area of research for various applications in the strategic sectors. Amongst the various existing AM techniques for production of maraging steels, Laser Powder Bed Fusion (LPBF) is the most widely used additive manufacturing technology for printing of complex-shaped components.

Optimization of processing parameters in LPBF additive manufacturing is most vital to obtain sound deposits and hence in achieving the final properties. TaoPeng et al. [3] investigated on Energy density in LPBF processing of materials. The low and high energy density resulted in larger and more pore formation, and the influencing parameter was laser power, followed by layer thickness, scan speed, and hatch space. SL Sing et al. [4] worked to overcome metallurgical defects in LPBF process such as pores, lack of fusion and intermetallic formations which can have detrimental effects on the performance of the parts. MahyarKhorasani et al. [5] investigated to identify how melt-pool temperature is determined by process parameters in LPBF. Taguchi design of experiments (DoE) was carried out to identify the effective process parameters influencing the in tensile properties including ultimate strength, fracture strain and toughness.

LPBF processing of M300 steels is considered in terms of several aspects, such as process parameter optimization to obtain high relative density, optimization of heat treatment to eliminate the anisotropic behavior and to improve mechanical properties. T. Silva et al. [6] investigated the Maraging steel produced by additive manufacturing under various loading conditions in order to understand behavior with respect to conventional material. Tests revealed very complex behavior of the maraging steels and the additive material showed higher tensile strength than the conventional material. Bai et al. [7] reported 400mm/s scanning speed and 160W laser power as the optimum process parameters to obtain higher than 99% relative density. Mutua et al. [8] reported that a laser power of 300W and a scan speed of 700mm/s resulted in a 99.8% maximum relative density. Król et al. [9] obtained a relative density of 99.3% with energy density at approximately 160J/mm^3. Tan Chaolin et al. [10] investigated a fully dense grade maraging steel 300 with optimum laser parameters and laser energy density of 67J/mm^3. Both SEM and EBSD analysis revealed a submicron grain size predicting an extremely high cooling rate up to 10^7K/s. Huang et al. [11] reported that a range of energy density between 75J/mm^3 and 185J/mm^3 could yield a relative density of more than 99%. RangasayeeKannan et al. [12] investigated the evolution of solidification texture during LPBF of Ti-free grade 300 Maraging steel, and its effect on texture development during subsequent post-fabrication heat treatments using EBSD characterization. NikiNouri et al. [13] developed a novel maraging steel for AM by PBF-LB and studied for suitable process parameters by means of single tract melt pool analysis.

JyotiSuryawanshi et al. [14] has investigated the tensile anisotropic behavior of the M300 specimen produced by AM in both as-deposited and heat-treated conditions and concluded that anisotropic properties in as-built specimens disappear after heat treatment. High cooling rates in LPBF (10^3–10^8K/s) make the microstructure anisotropic to the building direction. The as-deposited M300 specimens do not have required final strength and toughness. After aging treatment at optimized temperature and time, the highest mechanical properties were achieved by various researchers such as Bai et al. [7]; Casati et al. [15]; Kempen et al. [16].

The present study was aimed at identifying the window of process parameters and also optimized parameters for obtaining sound and defect-free deposits in LPBF additive manufacturing of Maraging steel. Additionally, the study also explores the effect of solutionizing treatment and aging heat treatment on microstructural and mechanical properties of AM processed M300 specimens. The effect of build orientation on the tensile properties is also evaluated.

2. Materials and Methods

2.1. Additive Manufacturing of Cubes and Tensile Specimens

Additive manufacturing of Maraging Steel M300 cubes and cylindrical specimens was carried out using the STLR-400 metal LPBF facility from M/s Amace Solutions Pvt. Ltd., Bengaluru. Maraging steel spherical powder M300 from Indo-MIM, Bengaluru was used for 3D printing of specimens. The spherical powder was produced by Indo-MIM using Inert gas atomization process.

Laser power, scan speed and hatch width play a dominant role during LPBF processing of alloys in determining the

melting of powders and continuity of solidified deposit across the scan vectors and inter-layers. In order to identify the parametric window for defect-free deposit, two crucial parameters, Laser power and Scan speed were chosen to vary across a wide range to identify the window of defect-free processing zone. Full factorial Design of Experiments (DoE) with 2 parameters and at 3 levels were considered to process 9Nos. [F1 to F9] of cube specimens ($10\times10\times10mm^3$) and deposited with process parameters as shown in Figure 1 and Table 1 respectively. Hatch width was chosen to be 80µm for all the process parameters. Scan strategy was kept bi-directional (zig-zag) within the stripe in a single layer. The scanning pattern was selected to move from left to right, i.e., against the direction of gas flow and the next layer was rotated 67° to the previous layer to minimize the residual stresses. The specimens were printed in an atmosphere of Nitrogen gas flow.

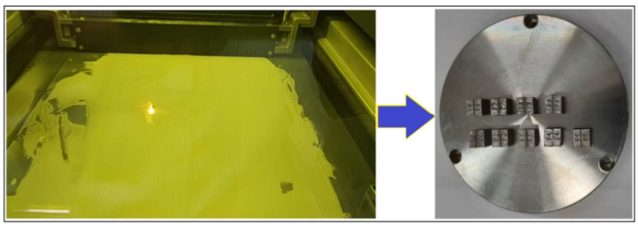

Figure 1. *LPBF-Printing of specimens (left) and printed specimens (right).*

Table 1. *Process Parameters of Laser deposited samples.*

Sample No.	Laser Power (Watts)	Scan Speed (mm/sec)
F1	100	500
F2	100	800
F3	100	1100
F4	200	500
F5	200	800
F6	200	1100
F7	300	500
F8	300	800
F9	300	1100

After the initial evaluation of 9Nos. of cube specimens, the primary process parameters in respect of laser power and scan speed were identified and additional 6Nos. of cube specimens were printed with varying hatch width and scanning pattern and studied to arrive at optimal parameters. Further, 12Nos. of cylindrical specimens (10mm dia, 75mm length) were printed using the optimized parameters in the horizontal orientation and 2Nos. in vertical orientation to evaluate the tensile properties.

The cubes and cylinders were subjected to heat treatment in two different conditions for evaluation, i.e. (a) Solution treatment (ST) at 840°C for 1hr., (b) Solution treatment + Aged (STA) at 490°C for 6hrs. Subsequently, microstructure and mechanical properties were evaluated on the as-deposited (AD), ST and STA conditions.

2.2. Chemistry and Metallographic Examination

Chemical analysis of powders and AM specimens was carried out on Inductively Coupled Plasma Optical Emission Spectroscopy (ICP-OES), Ultima Expert (HORIBA, France SAS make).

The specimens were sectioned by EDM wire cut machine, hot-mounted and grinding was carried out with SiC papers from 220 to 1200 grit sizes. The diamond paste was used in a sequential manner with particle sizes of 9, 3 & 1µm to attain mirror-polished surfaces. Optical micrography (OM) of these mirror-finished specimens was carried out on Leica-DM-6000M to obtain images for porosity evaluation. Finally, polished specimens were etched with the 3% Nital (97ml ethanol & 3ml nitric acid) solution to reveal the internal microstructure. Further, microstructural examinations were carried out using optical microscopy and Scanning Electron Microscope (SEM- ZEISS SUPRA 55) on AD, ST& STA specimens to observe the melt pool boundaries, sub-grain structure, micropores, inclusion, spatters, and other defects. Energy-dispersive X-ray spectroscopy (EDX) was performed at selected spots to determine the chemical elements and their relative abundance.

2.3. Porosity Analysis and Determination of Micro-Hardness

Porosity analysis was carried out to determine the overall pore content in the specimens using Image analysis technique. Initially, optical micrographs of polished specimens in AD condition were used to determine the porosity of the specimens using ImageJ software tool. Area fraction of pores and LoF defects were identified and estimated for at least 20 images across the specimen in horizontal and vertical directions to determine their volume fraction.

Micro-hardness and elastic modulus measurements were conducted on both AD and STA conditions on etched specimens using instrumented micro-indentation tester (Anton Paar make). Sufficient care was taken to perform indentation in the middle region of the melt pool in the build direction to obtain the hardness profile across the length of the specimen. A Vickers diamond pyramid indenter was used to apply a 10N load with loading and unloading rates of 20N/min and a pause of 10secs after loading.

2.4. Tensile Property Evaluation

Round tensile specimens were machined from AM deposited cylindrical specimens as per ASTM-E8 standard with a gauge length of 20 mm and dia 4mm. Walter-Baig testing machine equipped with an extensometer was used to perform the tensile tests. Extensometer was kept within extended length (28mm) for the test, and the displacement rate was set at 0.5mm/min. The test data was evaluated to obtain the mechanical properties such as yield strength (YS), ultimate tensile strength (UTS), & elongation (%El).

3. Results and Discussions

3.1. Chemical Analysis

The chemical composition of the Maraging steel M300 powder and the Laser deposited specimens in weight percentage are shown in Table 2.

Table 2. *Chemical composition of M300 powder and LPBF specimens.*

Element	ASTM A538M300	M300 Powder	LPBF specimen
C	≤0.03	0.02	0.02
Si	≤0.10	0.17	0.15
Mn	≤0.10	0.04	0.03
P	≤0.01	0.0022	0.002
Cr	≤0.50	0.27	0.18
Mo	4.60-5.20	5.16	5.10
Ni	18.0-19.0	18.6	18.1
Ti	0.50-0.80	0.78	0.71
Al	0.05-0.15	0.0054	0.005
Co	8.50-9.50	9.50	9.1
Fe	Bal	Bal	Bal

3.2. Identification of Process Parameters Window

During the AM processing of powder, imperfections such as pores, cracks, and cavities would occur if the optimized process parameters are not used. These defects lead to the reduction of the relative density (or increase in porosity) of the component. Initially, full factorial design of experiments (DoE) with 2 processing parameters [Laser power and Scan-speed] at 3-levels was used to arrive at the primary processing parameters for LPBF deposition of M300. Volumetric energy density (E_d) is an important guiding parameter for assessing the process optimization as it incorporates laser power, scan speed, hatch distance, and layer thickness, which is calculated by:

$$E_d = P/ (v \bullet h \bullet t)$$

Where E_d is energy density (J/mm^3), P is laser power (W), v is laser scan speed (mm/s), h is hatch distance (mm), and t is layer thickness of the powder bed (mm).

Figure 2 shows the representative images of the polished sections of the deposited specimens. Table 3 shows the porosity levels in the deposited specimens determined using Image analysis technique.

From the Table 3 it can be observed that when the energy density is above 100J/mm^3, a continuous deposit with reduced LoF defects would be formed. This implies that the energy density provided in this range would completely melt the powder particles and enhances the fluid flow in the scan tracks. At lower energy densities i.e., from 30-80J/mm^3, insufficient melting of the powders and high levels of porosity were observed. At higher densities from 150-250J/mm^3, the powder was completely melted, however, very fine spherical porosity and powder spatter was observed. The lowest porosities (<0.3%) were observed in F5, F7 and F8 specimens.

Table 3. *Comparison of Porosity and Energy Density for specimens.*

Sample No.	Laser Power (W)	Scan Speed (mm/sec)	Porosity (%)	EnergyDensity (J/mm^3)
F1	100	500	1.83	83.33
F2	100	800	4.92	52.08
F3	100	1100	5.69	37.88
F4	200	500	0.60	166.67
F5	200	800	0.29	104.17
F6	200	1100	0.95	75.76
F7	300	500	0.12	250.00
F8	300	800	0.18	156.25
F9	300	1100	0.44	113.64

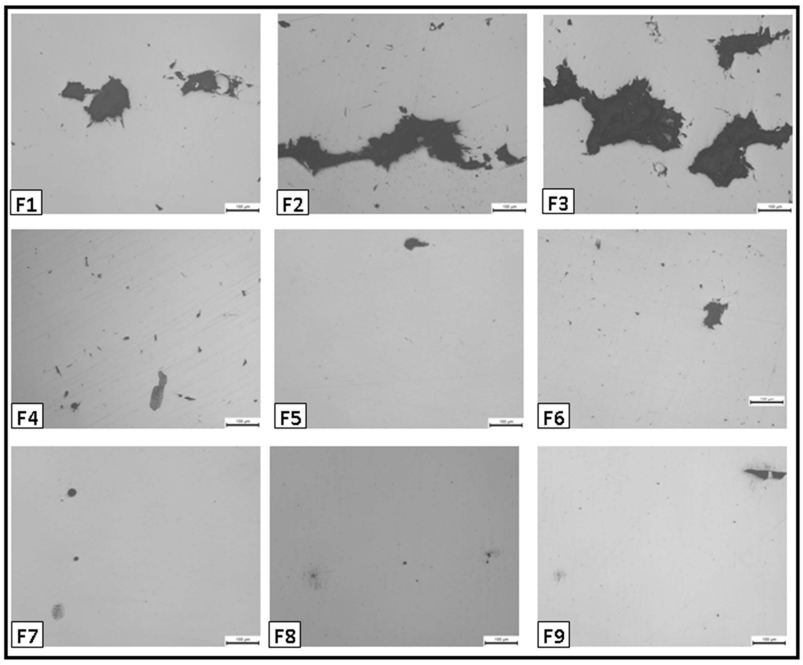

Figure 2. *Representative images of polished sections of deposited specimen.*

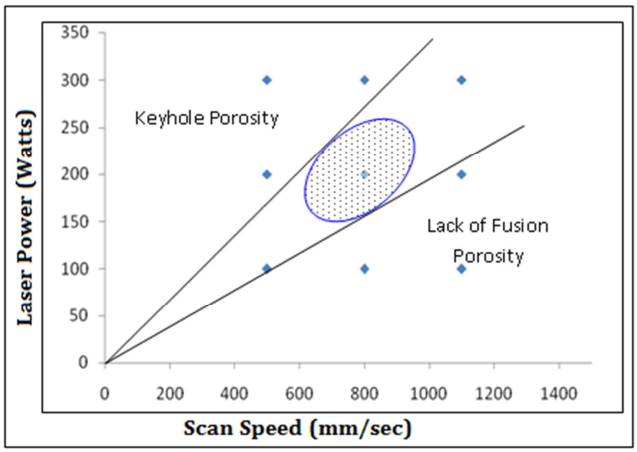

Figure 3. *Derived Process window for AM processed M300.*

However, in F7 and F8 specimens, imparting higher energy density to the powder has resulted in the formation of keyhole defects. These defects are typically formed due to increase in the melt pool depth created by the laser beam resulting in a pore like defect during solidification of the liquid metal. Furthermore, high energy density would also lead to high spatter of powder particles during deposition which will end up as metal condensate in the form of powder soot in solidified deposits. This type of defects is detrimental in attaining the desired material properties and hence parameters pertaining to Energy density of ~100J/mm^3 (specimen F5) were considered for further study. From the obtained results, a process window has been arrived at as per the Figure 3 shown below for additive manufacturing of Maraging steel M300. The elliptical shaded portion denotes the region with an energy density of about 100J/mm^3, which is most suitable for optimal AM processing of Maraging steel. The regions of defects like Keyhole porosity and LoF porosity also have been indicated.

3.3. Microstructural Analysis

3.3.1. Defect Analysis

Further analysis has been carried out on F5 specimen at high magnification imaging using optical microscopy (OM) and Scanning electron microscopy (SEM) to observe for the various microstructural features.

Figure 4 shows the optical micrographs of LPBF-deposited M300 at various magnifications in the direction normal to build direction. Micrographs exhibit semi-cylindrical melt pools formed because of localized and rapid solidification of the M300 powder bed. The width of the semi-cylindrical melt pool is between 110–130µm, equal to ~1.5times of laser beam diameter (80µm), and melt pool depth is approximately 50-60µm. The size of the melt pool depends on various process parameters such as laser power, laser beam diameter, and exposure time [15].

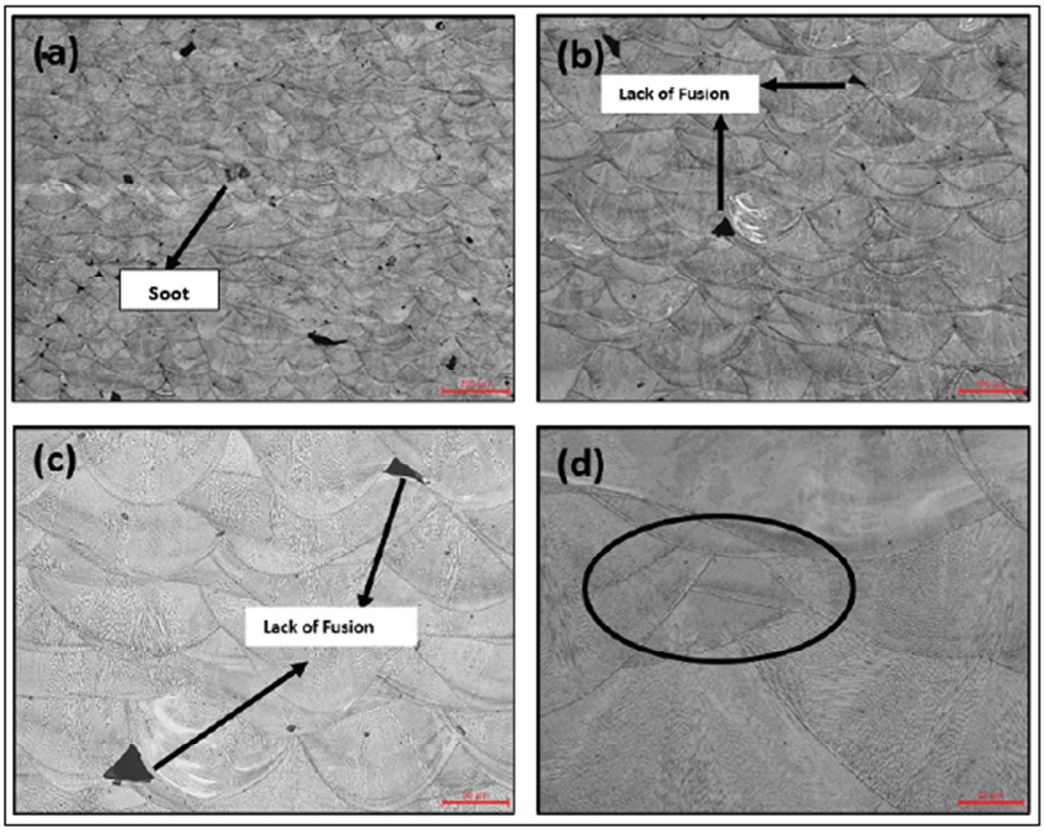

Figure 4. *LPBFOptical micrographs of as-built M300 steel at (a) 50X, (b) 100X, (c) 200X (d) 500X.*

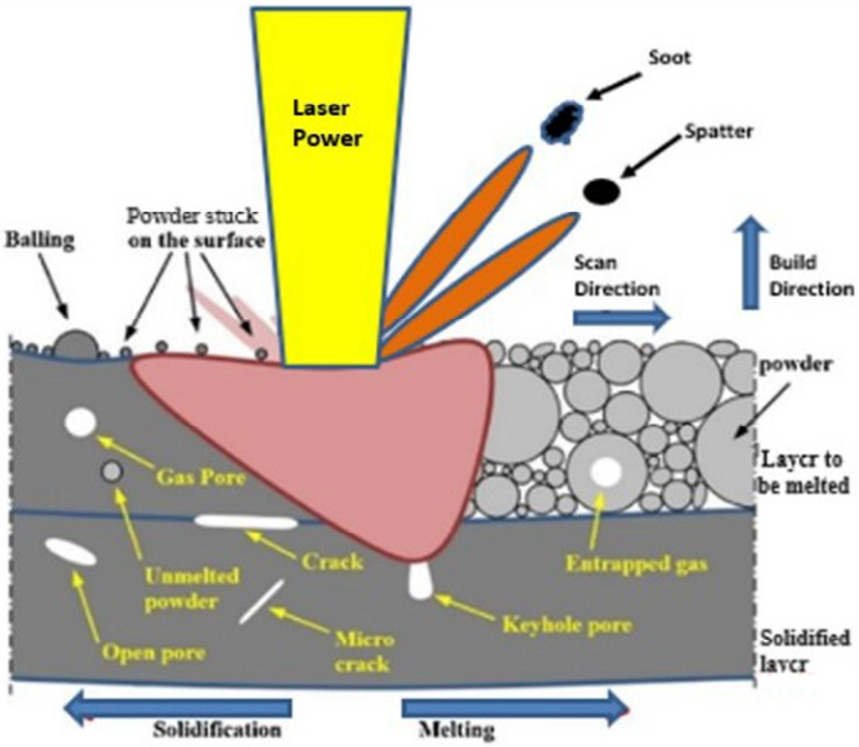

Figure 5. *Illustration of defect formation in laser-powder interaction Courtesy: Yakout et al. [17].*

The overlapping observed amongst melt pools in Figure 4 (d) is due to the hatch width of 80µm that helps in avoiding the interlayer porosity. In Figure 4 (a-c) dark triangular regions (20-30µm) can be observed along the vicinity of melt pools which are defects formed due to improper melting of powder. The existence of these defects is a critical issue as it prevents the LPBF printed component from achieving full density and decreases the mechanical properties. Yakout et al. [17] also reported more spatter formation during the LPBF process of Maraging steel as compared to other materials. Figure 4 (a) shows soot that forms due to evaporation of fine powder particles and settling on the surface, and (b, c) shows the lack of fusion defects marked by the arrow, which forms during the laser scanning. LoF defects mainly occur due to an insufficiency of energy which causes incomplete melting of metal powder and poor bonding between layers.

Figure 5 gives the illustration of various defects formation in additive manufacturing [17].

In Figure 6 arrow mark indicates pores and spatter. Pores are usually spherical which are formed because of the trapping of gas (initially present between metal powders) in the melt pool during rapid solidification [7]. Spatter forms during the LPBF process due to the ejection of metal powders or unstable molten particles from the melt pool [17]. The presence of metallic vapour and gaseous bubbles makes the melt pool unstable and cause the ejection of the unstable molten particle as a spatter. Figure 6 depicts the defect marked in the red circle caused by a large spatter.

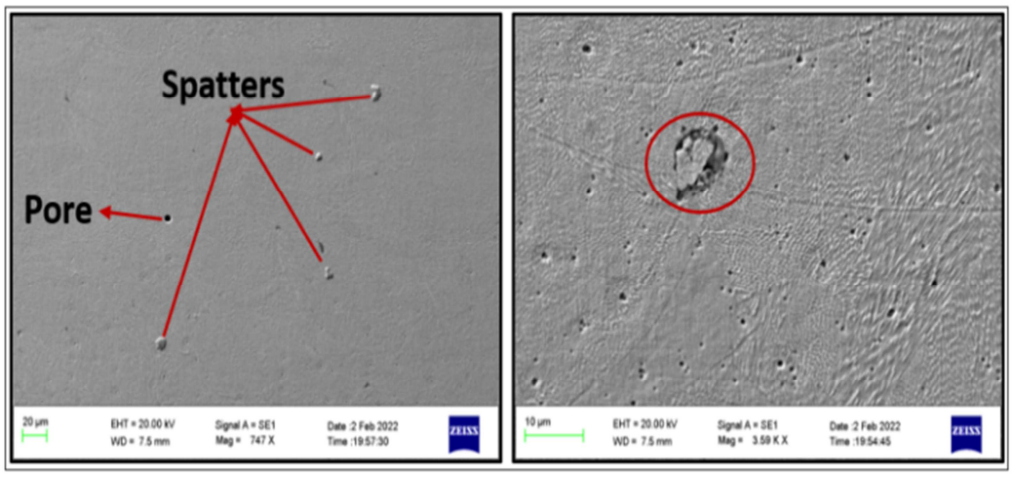

Figure 6. *SEM micrograph pores & spatter formed at 750X (left) and 3500X (right).*

Both small and large spatter ejection occurs during scanning, of which the small one gets dissolved by melting during scanning. However, big spatters stays as an impurity on the surface if the energy is insufficient to melt them completely, which further do not have a proper bonding with the surrounding layers and leads to internal defect.

3.3.2. Microstructure Analysis

The complicated thermal processes of the LPBF process lead to the formation of fine-grained cellular solidification structure and epitaxial growth across different track boundaries in the as-deposited (AD) condition. Figure 7 (a) SEM micrograph depicts two different cellular morphologies, cellular columnar and fine equi-axed cellular structures of less than 1µm in diameter. Besides, these cellular sub-grain structures within a grain are interspersed by the melt pool boundaries. This complex microstructure was attained due to the high cooling rates (about 10^6-10^8 K/s) experienced by the melt pool during LPBF process. A high cooling rate leads to rapid solidification due to severe temperature gradient and hence, prevents the formation of the lath martensite. The ratio of thermal gradient and the solidification rate determines the microstructure; the cellular structure forms along the direction of heat flow [10]. In Figure 7 (b) arrow marks indicate the epitaxial growth of cellular grain across the melt pool boundaries. Partial re-melting of adjacent beads occurs during the laser scanning process, which permits the new grain to form with the identical crystallographic orientation of nearby grains [16].

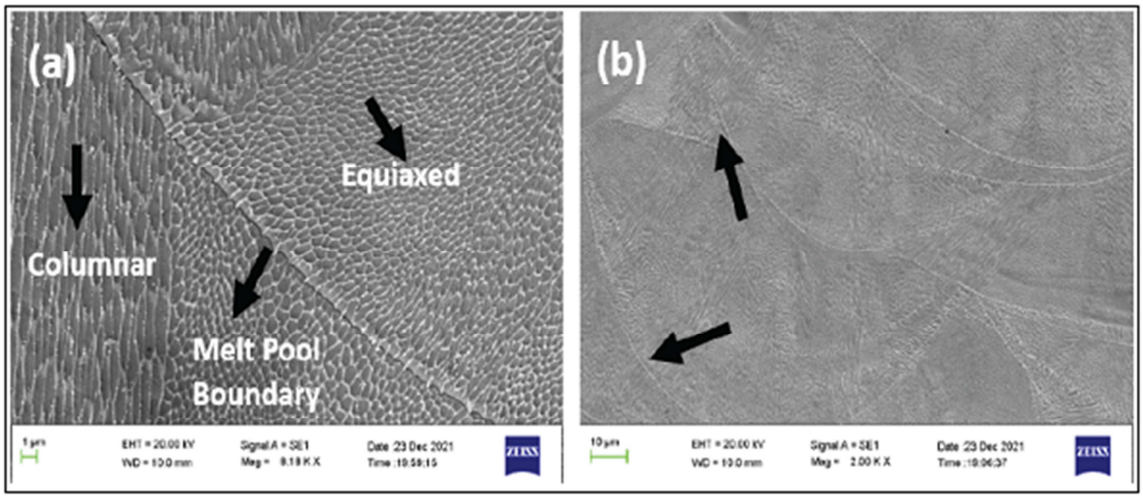

Figure 7. *SEM micrographs of AD specimen.*

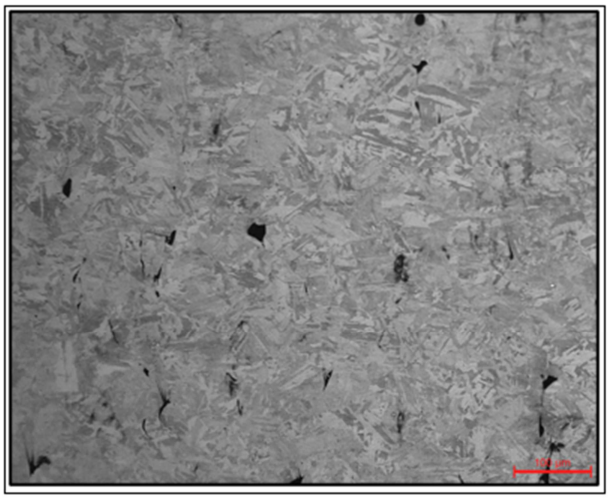

Figure 8. *Micrograph of ST specimen at 100X.*

As shown in Figure 8, microstructure of the solution treated (ST) specimens at 840°C for 1 hr., revealed that cellular structures and melt pools have completely disappeared due to their dissolution at high temperatures into the austenitic regime. When cooled back to RT, the obtained microstructure is understood as Martensite blocks or pockets which replaced the former cellular structure. Ahmadkhaniha et al. [18] and Tan et al. [10] also observed a similar microstructural change by solution treatment.

Direct-aging (DA) of as-deposited specimen (490°C for 6hrs), has been carried out to assess the difference in the microstructure as compared to ST condition. The Figure 9 shows a distinct microstructure from that of the solution treated condition. The cellular structure from the AD condition becomes blurred but does not disappear completely, as seen clearly in Figure 9. A black arrow marks the blurred melt pool boundary, and columnar and fine equiaxed structures are marked in yellow and black circles respectively in Figure 9. As austenite is already present at cell boundaries (bright constituent in figure), they act as nucleation sites for their further growth due to enrichment of Ni, which reduces austenite transformation temperature.

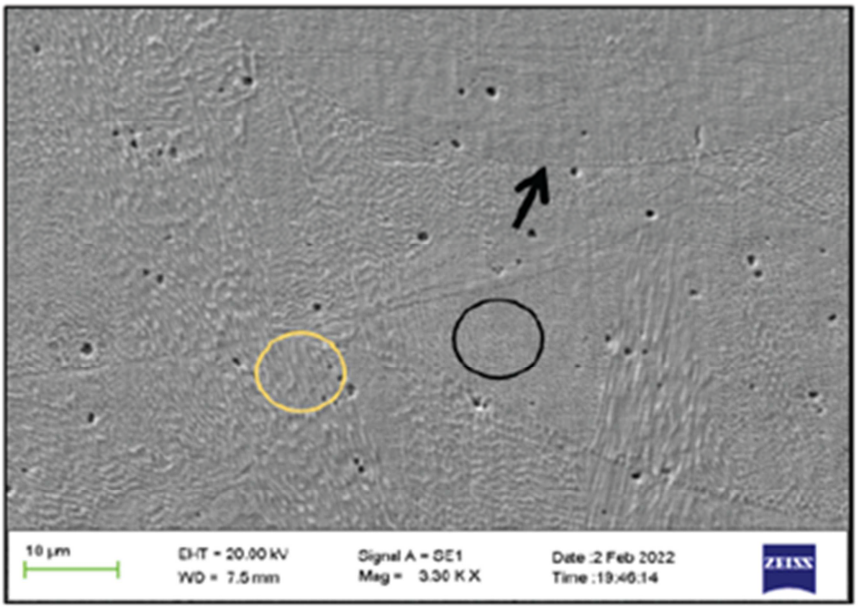

Figure 9. *SEM Micrograph of the DA specimen.*

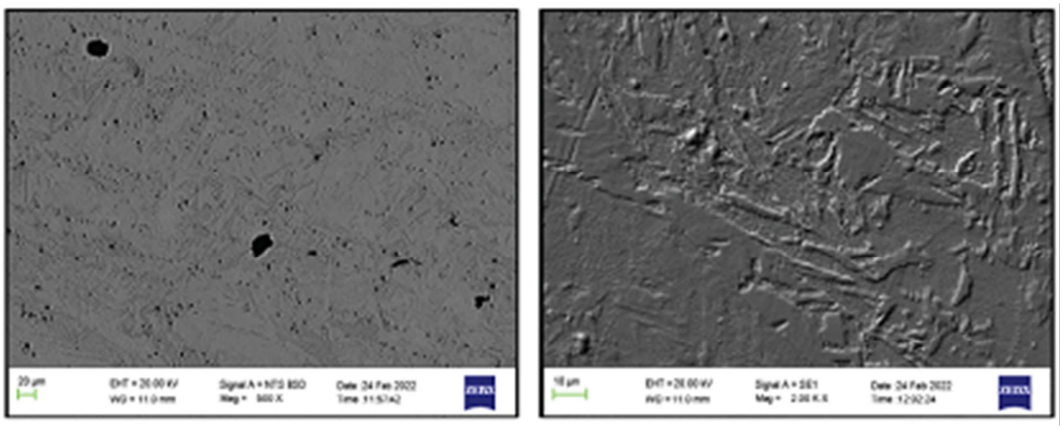

Figure 10. *SEM micrographs at 500X and 2000X of STA specimen.*

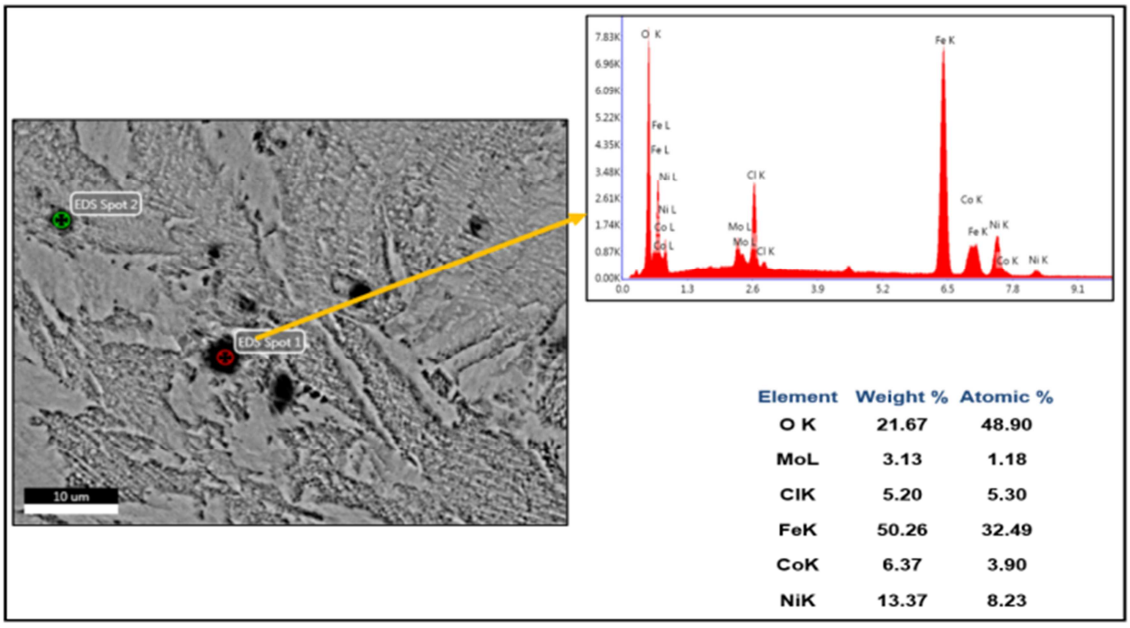

Figure 11. *EDX result showing elemental composition at marked spot.*

Microstructure of solution treated (at 840°C for 1 hr.) and aged (at 490°C for 6hrs.) specimens (STA) are shown in Figure 10. The microstructure is entirely different from DA specimen. Martensite laths were observed instead of cellular structures and were denser and thinner with sharp boundaries [18]. Presence of rounded dark particles was observed in STA specimens when examined using SEM and energy-dispersive x-ray spectroscopy (EDX). Figure 11 shows EDX analysis carried out on a dark rounded particle which shows that, the atomic percent of iron & oxygen to be 32 & 48 respectively, indicating formation of Fe_2O_3 particles.

3.4. LPBF Printing with Modified Process Parameters

From the micro-structural analysis of F5 specimen at high magnifications, it was revealed that even at the process parameters pertaining to F5, one could still observe the formation of powder spatter, soot and micro level LoF defects. In order to minimize these defects of soot and spatter, 6Nos. of specimens (M1 to M6) were printed with modified parameters of hatch width and scanning pattern to study their effect on the porosity. The laser power and scan speed were slightly modified within the identified window (Figure 3) to increase the melting temperature of powders and reduce the LoF defects. The former F1-F9 specimens were printed using zig-zag scanning pattern, i.e. the scan vector scans in a bi-directional way in a stripe region. In the current specimens M1-M3 were printed using zig-zag scanning pattern and for M4-M6 the scanning pattern is kept in zig-zig mode, i.e. the scan vector moves only in a single direction within a stripe region. The Table 4 depicts the modified parameters used and the observed porosity and calculated energy density for M1-M6 specimens.

Table 4. *Comparison of Porosity and Energy Density for specimens.*

Sample	Power (W)	Scanspeed (mm/s)	Layer Thk (µm)	Hatch (mm)	Scan pattern	ED (J/mm^3)	Porosity (%)
M1	200	835	30	0.12	zig-zag	66.5	0.65
M2	230	835	30	0.12	zig-zag	76.6	0.33
M3	210	835	30	0.10	zig-zag	83.8	0.15
M4	210	835	30	0.08	zig-zig	104.8	0.12
M5	200	835	30	0.12	zig-zig	66.5	0.56
M6	200	835	30	0.10	zig-zig	79.8	0.32

From the above Table 4, it can be noted that the least porosity (0.12%) is obtained for M4 specimen printed with zig-zig pattern and 0.08 mm hatch width. From Figure 12, a pattern can be observed that relative density increases with an increase in energy density. The high value of energy density melts powder properly, reduces the possibility of lack of fusion, and ensures strong metallurgical bonding between layers.

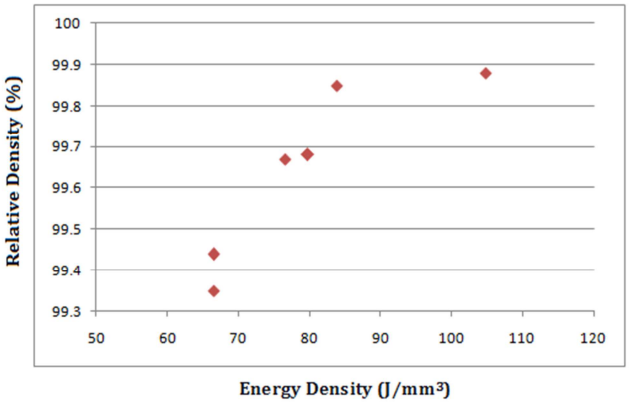

Figure 12. *Plot showing variation of relative density with energy density.*

The result obtained is in agreement with the results of Bai et al. [7] that the hatch space has a critical role in relative density and which was kept least in the M4 specimen. Hatch space is related to overlapping; if it is more, there is a possibility of inadequate fusion between adjacent scan tracks. Conversely, if hatch space is less, more number of points in the solidified are re-melted, which reduces the porosity.

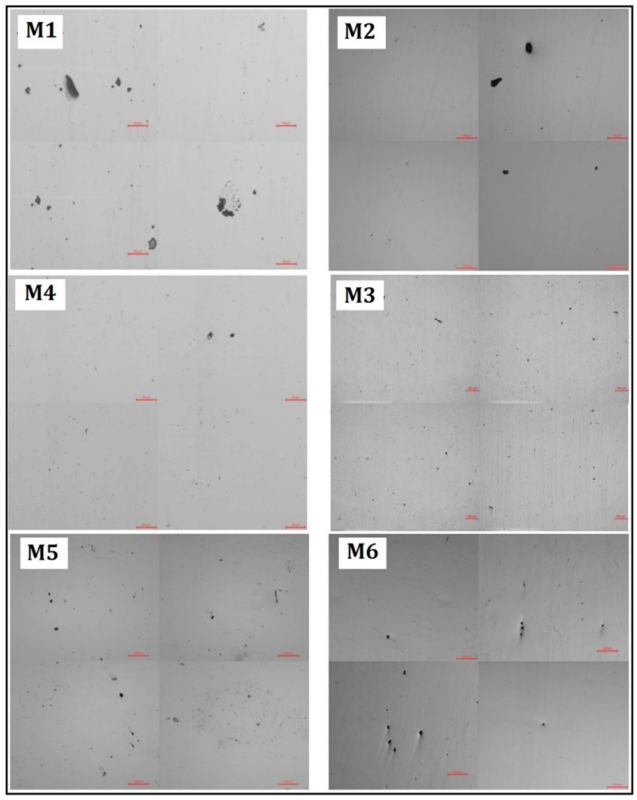

Figure 13. *Stitched micrographs (50X) of as-deposited M1-M6.*

From the Figure 13 it is also seen that M4 specimen is found to have reduced soot and spatter compared to F5 specimen printed with zig-zag pattern.

This effect of the scanning pattern (zig-zig vs zig-zag) on deposits can also be explicitly observed by comparing M1 and M5 specimens. These two specimens were printed with the same process parameters and energy density except for the scanning pattern. Zig-zig type of scanning pattern showed reduced spatter and soot in the M5 specimen when compared to that of M1 specimen which was deposited using zig-zag pattern. It may be due to burnt soot particles being carried away by the gas flow when scanned in zig-zig pattern and prevents them from settling in the nearby zones which are yet to be scanned. This could be the possible reason for better relative density (or reduced porosity) with reduced formation of soot compared to the zig-zag scanning pattern.

From the comparison of Table 3 and Table 4, the F1 and M3 specimens were printed with similar energy density values but with varied laser power and scan speed parameters. Nevertheless, the porosity values were found to be drastically different, i.e. 1.83 and 0.15 respectively for F1 and M3 specimens. This clearly indicates that Energy density is a necessary but not a sufficient parameter to completely assess the sound condition of the deposits in AM. The other process parameters also need to be considered while optimizing the parameters for obtaining a sound deposit in AM.

3.5. Mechanical Properties Evaluation

The M4 specimen which has resulted in low porosity due to reduced formation of soot was further studied for different mechanical properties (Hardness, elastic modulus and tensile) in different heat treated conditions.

3.5.1. Determination of Micro-Hardness and Modulus

The comparative hardness and elastic modulus values of the as-deposited and solution treated & aged specimens with respect to distance from top to bottom in the build direction are given in Figure 14.

After solution treatment & aging treatment, significant improvement in hardness and elastic modulus was observed. Aging for 6 hours at 490°C improved the hardness to 600-630 (615±7) HV from 400-450 (430±13) HV in as-deposited condition. This improvement in hardness was mainly due to the formation of nano-precipitates during aging, which is the primary strengthening mechanism of maraging steel. During aging treatment, alloying elements like Ni, Ti, and Mo dissolved in the martensitic matrix precipitate out to form intermetallics such as Ni_3Ti, Ni_3Mo, Fe_7Mo_6 and Fe_2Mo. These second phase precipitates hinder the dislocation movement and lead to the strengthening of the matrix [19]. Results also depicted the improvement of elastic modulus from 145-150GPa to 165-175GPa, which is consistent with the result obtained by Kempen et al. [16]. The reason is ascribed to the depletion of nickel in the martensitic matrix due to the formation of $Ni_3(Mo,Ti)$ precipitates.

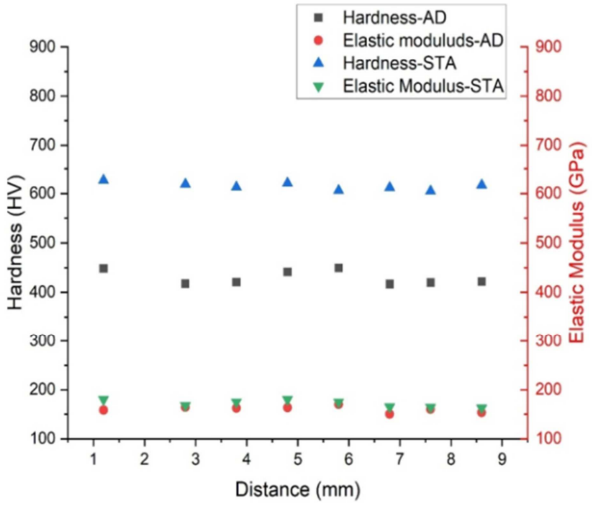

Figure 14. *Micro hardness and Modulus of AD & STA specimens.*

3.5.2. Tensile Test Results

The Figures 15, 16 & 17 depict the uniaxial tensile stress vs. strain graphs of specimens built in horizontal direction in as-deposited (AD), solution treated (ST), and solution treated and aged (STA) conditions. Table 5 gives the Tensile test results of AD (horizontal, AD-H), ST (horizontal, ST-H), STA (horizontal, STA-H & vertical, STA-V) specimens.

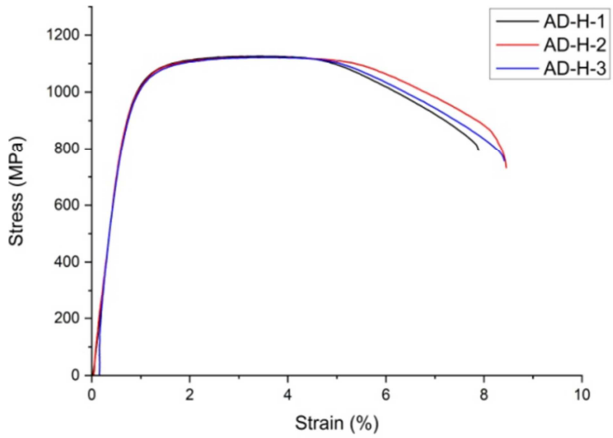

Figure 15. *Stress-strain curve of horizontally built AD specimen.*

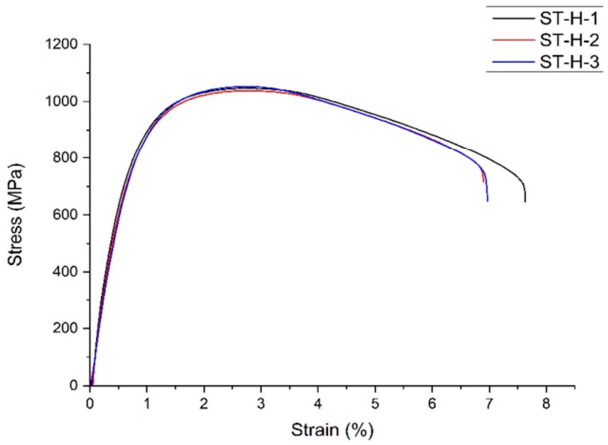

Figure 16. *Stress strain curve of horizontally built ST specimen.*

Table 5. *Tensile test results of AD (H), ST (H), STA (H) & STA (V) specimen.*

Sample	0.2%YS (MPa)	UTS (MPa)	Elongation (%)	RA (%)
AD-H-1	1001	1126	12.8	47.3
AD-H-2	994	1123	11.2	46.2
AD-H-3	989	1122	10.8	50.2
ST-H-1	788	1047	13.09	48.1
ST-H-2	793	1038	12.98	42.7
ST-H-3	818	1053	13.23	49.2
STA-H-1	1954	2001	OGL	_
STA-H-2	1919	1956	OGL	_
STA-H-3	1907	1971	OGL	_
STA-H-4	1957	2020	2.8	18.2
STA-H-5	1878	1911	2.3	18.1
STA-H-6	1814	1904	OGL	_
STA-V-1	1591	1871	2.7	11.2
STA-V-2	1635	1900	2.8	17.2

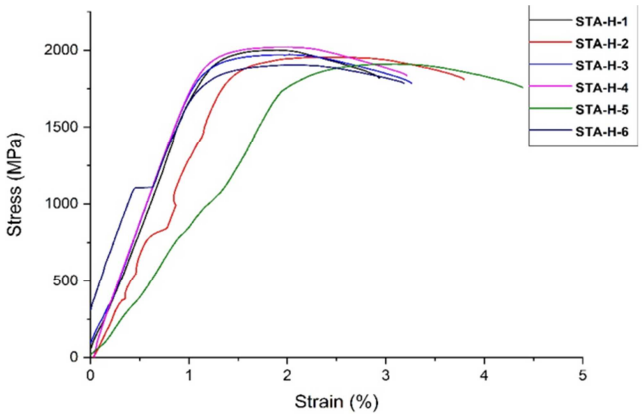

Figure 17. *Stress-strain curve of horizontally built STA specimen.*

It can be observed from Table 5 that the ST specimens have lower strength (average YS=800MPa) than the AD specimen (average YS=995MPa). AD specimens have fine-grained martensite because of the rapid solidification of the melt pool at high cooling rates. Moreover, in the as-deposited specimens, there are residual stresses, which prevent the motion of dislocations [20]. However, solution treatment results in change of fine grained structure into lath martensite and martensitic transformation is proportional to temperature and holding time. A reduction of approximately 10% tensile strength has been observed in ST specimens, possibly because of the elimination of fine structure and residual stresses after solution treatment. Tan et al. [10] also observed a similar reduction in strength and the reason ascribed to the presence of soft and deformable martensite after solution treatment.

However, after the aging treatment, tensile strengths of solution-treated specimens increase sharply to 1900-2000MPa, as shown in Figures 17, 18. Increase in strength was mainly due to the formation of intermetallic nano sized precipitates such as Ni_3Ti, Ni_3Mo, Ni_3Al, and Fe_2Mo [10] in high volume fractions. Compared to direct aging (DA), solution treatment and aging (STA) specimen should attain higher tensile strength because of the lower volume fraction of reverted austenite present in the STA condition. In contrast, a decline in ductility can be observed after aging treatment. From the Table 5, it can be observed that elongation was reduced from over 13% to less than 3% after ageing treatment. The strengthening of the martensitic matrix by intermetallic precipitates results in reduced ductility, which is a characteristic feature of aged maraging steels.

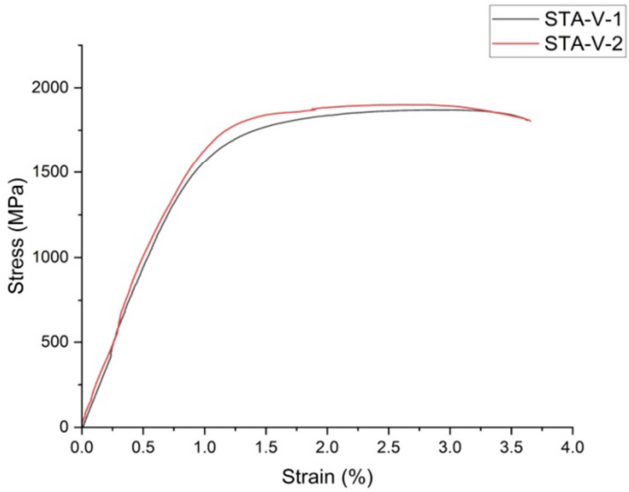

Figure 18. *Stress-strain curve of verically builtSTA specimen.*

The average YS and UTS of horizontally printed (STA-H) specimens are 1905MPa and 1960MPa, respectively. The YS and UTS of vertically printed (STA-V) specimens are 1613MPa and 1886MPa, respectively, Figure 18.

The difference in YS and UTS of STA-H is 2.9%, but for STA-V, it is 16.9%. Hence, it can be concluded that plastic deformation starts at an early stage and deform over a wide range of load in STA-V than in STA-H. In vertically built specimens, the load is applied parallel to the building directions, and in the horizontally built specimens, the loading direction is perpendicular to building direction. Therefore, cracks and voids between layers in the vertically printed specimens are more likely to act as stress risers and produce a drop in the tensile strength. Hence, it can be understood that AM processing of M300 in horizontal orientation is preferred to attain higher tensile properties.

Table 6. *Comparison of tensile results with wrought sample.*

Building orientation	Specimen	YS (MPa)	UTS (MPa)	Elongation (%)
	AD	995±5	1124±2	11.6±0.9
Horizontal	ST	800±13	1046±6	13.1±0.1
	STA	1905±49	1961±43	2.6±0.3
Vertical	STA	1613±22	1886±15	2.8±0.05
	Wrought	760-895	1000-1170	6-15
	Wrought-Aged [10]	1862-2000	1930 - 2050	5-7

From Table 6, the tensile strength of AD is on the higher side compared to that of wrought specimen which can be attributed to the effect of intrinsic heat treatment in the AM process, resulting in precipitation of intermetallics. When the laser melts a track, a part of the heat is absorbed by the neighboring zones, and the adjacent solidified material would be reheated to high aging temperatures, which facilitates precipitation of intermetallics. This phenomenon is known as intrinsic heat treatment, characteristic to AM process due to layer-by-layer method of manufacturing. Further, it can be noted that the STA specimen has comparable strength with that of wrought-aged specimen, however the elongation values are found to be 50% less. This reduction in elongation may be attributed to the presence of micro-voids, oxides and nitrides formed in the deposits which accentuate the propagation of cracks.

Further work involves investigation into the volume fraction of reverted Austenite and its effect on the mechanical properties of AM processed Maraging steel. Study related to joining of AM processed M300 to the conventional Maraging steel material is also a relevant area to be carried out.

4. Conclusion

Following conclusions were drawn from the present study:

Full factorial DoE was used to arrive at the primary processing parameters viz. Laser Power-200W, Scan speed-800mm/sec, Hatch width-80µm for AM of Maraging steel. A process window comprising of Laser power & scan speed has been identified corresponding to the region with an energy density of about 100J/mm^3, to obtain sound deposits.

Microstructure of AD specimens observed to be comprised of melt pool boundaries, epitaxial growth of short columnar grains across the layers and the fine cellular structure (<1µm) within the grains. This unique structure vanished completely after solution treatment, and in the subsequent aging treatment thin martensitic lath structures were formed. Moreover, SEM analysis at high magnification revealed the presence of powder spatter, soot and micro LoF defects in the AD condition.

Consequently, specimens printed with a modified scanning pattern from zig-zag to zig-zig, has further minimized the formation of soot and spatter in the deposit. At the optimized parameters of laser power-210W, scan speed-835mm/sec, hatch width-80µm with zig-zig pattern, a minimum porosity of 0.12% was obtained. Besides, Energy density is found to be a necessary but not a sufficient parameter to obtain sound deposits in AM.

Microhardness along the build direction of AD specimen was determined to be 430±13 HV, whereas in STA condition, the hardness increased upto 615±7 HV, attributed to the precipitation of nano-sized intermetallics.

The tensile strength of AD is on the higher side compared to that of wrought specimen which is due to the effect of intrinsic heat treatment inherent to AM process. The STA specimen has comparable strength with that of wrought-aged specimen, however, the elongation values are found to be lower by 50%. Reduction in elongation may be attributed to the presence of micro-voids, oxides and nitrides formed in the deposits which accentuate the propagation of cracks to failure.

YS and UTS of horizontally built specimens were determined to be on higher side than that of vertically built specimens in STA condition. Therefore, AM processing of Maraging steel in horizontal orientation is preferable to attain higher tensile properties and hence sections experiencing the load in a component are suggested to be printed in this orientation.

Acknowledgements

We are thankful to Director, DMRL for his constant support and encouragement in the activities related to Additive Manufacturing technology. We also thank M/s Amace Solutions Pvt. Ltd., Bengaluru for providing the facility to carry out the additive manufacturing of the specimens. Thanks are also due to other groups of DMRL viz., SFAG, EMG & MBG for extending necessary technical services.

References

[1] Mercedes Pérez, Diego Carou, Eva María Rubio & Roberto Teti. (2020). Current advances in additive manufacturing. 13th CIRP Conference on Intelligent Computation in Manufacturing Engineering, CIRP ICME '19, Procedia CIRP 88. 439–444.

[2] Brett P Conner, Guha P Manogharan, Ashley N Martof, Lauren M Rodomsky, Caitlyn M Rodomsky, Dakesha C, Jordan & James W Limperos. (2014). Making sense of 3D printing: Creating a map of additive manufacturing products and services, Additive Manufacturing, Vol 1-4, 64-76.

[3] Tao Peng& Chao Chen. (2018). Influence of Energy Density on Energy Demand and Porosity of 316L Stainless Steel Fabricated by Selective Laser Melting. International Journal of Precision Engineering and Manufacturing-Green Technology. Vol. 5, No. 1, 55-62.

[4] S. L. Sing & W. Y. Yeong. (2020) Laser powder bed fusion for metal additive manufacturing: perspectives on recent developments. Virtual and Physical Prototyping. 15: 3, 359-370, doi: 10.1080/17452759.2020.1779999.

[5] Mahyar Khorasani, Amir Hossein Ghasemi, Umar Shafique Awan, Sarat Singamneni, Guy Littlefair, Ehsan Farabi, Martin Leary, Ian Gibson, JithinKozhuthalaVeetil& Bernard Rolfe. (2021). On the role of process parameters on melt-pool temperature and tensile properties of stainless steel 316L produced by powder bed fusion. Journal of materials research and technology. 12. 2438-2452.

[6] T. Silva, F. Silva, J. Xavier, A. Greg´orio, A. Reis, P. Rosa, P. Konopık, M. Rund& A. Jesus. (2021). Mechanical Behaviour of Maraging Steel Produced by SLM", Procedia Structural Integrity. 34. 45–50.

[7] Bai, Y., Yang, Y., Xiao, Z., & z Wang, D. (2018). Selective laser melting of maraging steel: mechanical properties development and its application in mold. Rapid Prototyping Journal. 24 (3). 623–629.

[8] Mutua, J., Nakata, S., Onda, T. & Chen, Z. (2018). Optimization of selective laser melting parameters and influence of post heat treatment on microstructure and mechanical properties of maraging steel. Materials & Design. 139. 486–497.

[9] Król, M., Snopiński, P. & Czech, A. (2020). The phase transitions in selective Laser melted 18-NI (300-grade) maraging steel. Journal of Thermal Analysis and Calorimetry. 142 (2), 1011-1018.

[10] Tan Chaolin, Kesong Zhou, Min Kuang, Wenyou Ma & TongchunKuang. (2018). Microstructural characterization and properties of selective laser melted maraging steel with different build directions. Science and Technology of Advanced Materials. Vol 19, No. 1, 746–758, doi.org/10.1080/14686996.2018.1527645.

[11] Huang, W., Zhang, W. & Chen, X. (2020). Effect of SLM Process Parameters on Relative Density of Maraging Steel (18Ni-300) Formed Parts. IOP Conference Series: Materials Science and Engineering. 774 (1), 012027.

[12] Rangasayee Kannan& Peeyush Nandwana. (2022). Texture evolution during processing and post-processing of maraging steel fabricated by laser powder bed fusion. www.nature.com/scientificreports, Scientific Reports. 12: 6396. doi.org/10.1038/s41598-022-09977-1.

[13] NikiNouri, Qing Li, James Damon, FabianMu¨hl, Gregor Graf, Stefan Dietrich & Volker Schulze. (2022). Characterization of a novel maraging steel for laser-based powder bed fusion: optimization of process parameters and post heat treatments. Journal of materials research and technology. 18, 931-942.

[14] JyotiSuryawanshi, K. G. Prashanth & U. Ramamurty. (2016). Tensile, fracture, and fatigue crack growth properties of a 3D printed maraging steel through selective laser melting. Journal of Alloys and Compounds. 725, 355-364.

[15] Casati, R., Lemke, J. & Vedani, M. (2016). Microstructure and Fracture Behavior of 316LAustenitic Stainless Steel Produced by Selective Laser Melting. Journal of Materials Science & Technology. 32 (8), 738–744.

[16] Kempen, K., Yasa, E., Thijs, L., Kruth, J.-P. & Humbeeck, J. (2011). Microstructure and mechanical properties of Selective Laser Melted 18Ni-300 steel. Physics Procedia, 12, 255–263.

[17] Yakout, M., Phillips, I., Elbestawi, M. A& Fang, Q. (2021). In-situ monitoring and detection of spatter agglomeration and delamination during laser-based powder bed fusion of Invar 36. Optics & Laser Technology. 136, 106741.

[18] D. Ahmadkhaniha, H. Moller, & C. Zanella. (2021). "Studying the Microstructural Effect of Selective Laser Melting and Electropolishing on the Performance of Maraging Steel. Journal of Materials Engineering and Performance. Volume 30 (9), 6588-6605.

[19] Gao, P., Jing, G., Lan, X., Li, S., Zhou, Y., Wang, Y., Yang, H., Wei, K. & Wang, Z. (2021). Effect of heat treatment on microstructure and mechanical properties of Fe–Cr–Ni-Co–Mo maraging stainless steel produced by selective laser melting. Materials Science and Engineering: A, 814, 141149.

[20] Aydin, İ. (2020). Investigating effects of heat treatment processes on microstructural and mechanical properties of additively manufactured 18Ni300 maragingsteel. A thesis submitted to the Graduate School of Natural and Applied Sciences of Middle East Technical University.